Nuclear Instruments and Methods in Physics Research A 831 (2016) 370–377

Contents lists available at ScienceDirect

Nuclear Instruments and Methods in Physics Research A

journal homepage: www.elsevier.com/locate/nima

Diamond sensors for future high energy experiments

Felix Bachmair, On behalf of the RD42-Collaboration[1]

ETH Zürich, Institute for Particle Physics, Switzerland

ARTICLE INFO

Article history:
Received 20 November 2015
Received in revised form
9 March 2016
Accepted 11 March 2016
Available online 14 March 2016

Keywords:
CVD diamond
Diamond particle detector
Particle physics
Radiation hardness
3D sensors
Charge collection

ABSTRACT

With the planned upgrade of the LHC to High-Luminosity-LHC [1], the general purpose experiments ATLAS and CMS are planning to upgrade their innermost tracking layers with more radiation tolerant technologies. Chemical Vapor Deposition CVD diamond is one such technology. CVD diamond sensors are an established technology as beam condition monitors in the highest radiation areas of all LHC experiments. The RD42-collaboration at CERN is leading the effort to use CVD diamond as a material for tracking detectors operating in extreme radiation environments. An overview of the latest developments from RD42 is presented including the present status of diamond sensor production, a study of pulse height dependencies on incident particle flux and the development of 3D diamond sensors.

1. Introduction

With the planned upgrades of the Large Hadron Collider (LHC) to High Luminosity (HL-LHC) [1] and the next generation of particle physics experiments in development, new energy and luminosity regimes will be reached. The expected fluence for the inner most layer of the tracking detector at HL-LHC is $\Phi_{1\ \mathrm{MeV n_{eq}}} = 2 \times 10^{16}\ \mathrm{n_{eq}/cm^2}$ [2] and the flux is expected to be up to 1.5 GHz $/\mathrm{cm}^2$ [3, scaled to the expected instantaneous luminosity]. For these harsh radiation environments new technologies for tracking detectors are most likely required. With its large band-gap ($E_{gap} = 5.5$ eV at $T = 302$ K) and its high binding energy, diamond has ideal material properties to work as a particle detector in these environments. Chemical Vapor Deposition (CVD) diamonds have been shown to be at least three times more radiation tolerant [4], to have at least a two times faster charge collection [5], and to be four times more thermally conductive [6] than corresponding silicon detectors. Low leakage currents, low dielectric constant and the ability to work at room temperature are also appealing properties for tracking detectors.

The RD42-collaboration, based at CERN, is investigating the capability of diamond detectors in the field of high energy physics. The signal response of response of single-crystal CVD (scCVD) and polycrystalline CVD (pCVD) diamonds irradiated up to 1.8×10^{16} protons/cm^2 [7] has been measured, indicating that diamond-based detectors are good candidates for tracking detectors close to the interaction point. In order to increase the radiation hardness even further RD42 recently started to evaluate diamond detectors based on the new 3D geometry. As part of the mission, RD42 has been working with diamond manufacturers for two decades to improve the quality of artificially grown diamonds based on the (CVD) technique to make them suitable for use as charged particle sensors. For a long time only a single manufacturer [8] was capable of producing detector grade diamonds. In the last years two new producers, II-VI Incorporated [9] and IIa Technologies [10], have entered the market.

When comparing qualities of diamond sensors the figure of merit is the Charge Collection Distance (CCD), which is defined as the average distance an e/h-pair separates under the influence of an electric field [11]. In order to maximize the amount of collected charge and obtain the best possible signal, the CCD should be as high as possible. For a non-irradiated scCVD diamond full charge collection is expected, which means that the CCD is equal to the thickness of the diamond. For pCVD diamonds the CCD is expected to be lower than the thickness due to charge trapping.

The company II-VI Incorporated [9] has been producing laser windows based on pCVD diamonds for several years, and recently started to grow detector grade diamond material as well. In this time the quality of their pCVD diamonds has improved. They have delivered final finished parts (~ 100 parts of various sizes) to the particle physics experiments Compact Muon Solenoid (CMS) and A Toroidal LHC ApparatuS (ATLAS). The majority of their final finished diamond sensor parts now reach a CCD of 275–300 μm. In Fig. 1 the CCD of four preselected diamonds is shown as a function of bias voltage. All samples reach a CCD of above 300 μm at a bias voltage of 800 V, corresponding to an electric field of 1.5 V/μm.

E-mail address: bachmair@phys.ethz.ch
[1] Collaboration author list in Appendix.

http://dx.doi.org/10.1016/j.nima.2016.03.039

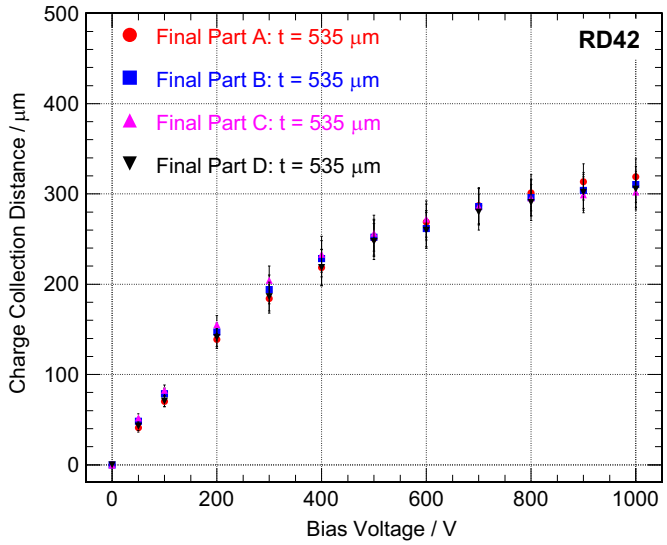

Fig. 1. The CCD as a function of bias voltage for four pCVD diamonds produced by II-VI Incorporated.

A second new company on the market is IIa Technologies [10]. They have delivered order of ten scCVD samples for evaluation, showing promising results.

RD42 is working with these companies to ensure that their diamonds have the necessary signal properties, uniformity and radiation tolerance. The appearance of additional manufacturers is encouraging. It has a positive effect on the quality of CVD diamonds and adds growth capacities.

2. Use of diamond detectors

In all experiments at the LHC there are detectors installed that use diamond as a sensor material. Several scCVD and pCVD diamond-based beam condition monitors for on-line background estimation and luminosity measurements are now in use in ATLAS [12,13], CMS [14,15] and LHCb [16].

The Pixel Luminosity Telescope (PLT) is designed to provide a bunch-by-bunch measurement of the luminosity for the CMS experiment. With the pixelated sensors particle tracking is possible. This allows us to distinguish collision products from beam background. During the LHC run in 2012 diamond pixel telescopes were employed in the pilot run of the PLT [15,17]. Four diamond telescopes, each telescope with three pixelated scCVD diamond detectors with an area of $4.5 \times 4.5\ \mathrm{mm}^2$ and a pixel size of $150 \times 100\ \mu\mathrm{m}^2$, were installed on the platform formerly housing a CASTOR detector [18] 14.5 m away from the collision point. In preparation for the final PLT installation, issues with these scCVD PLT diamonds (described in Section 3) created a situation where the timescale to complete the project was delayed. As a result the CMS collaboration decided to install a silicon based PLT and designed and added a full cooling system in order to meet the required installation deadline.

During the LHC shutdown in 2014, ATLAS installed the Diamond Beam Monitor DBM [19]. The purpose of the DBM is to provide a bunch-by-bunch luminosity and a bunch-by-bunch beam spot measurement. This is achieved by tracking individual particles using eight 3-plane pixel telescopes. Six of these telescopes use pCVD diamond sensors, each with a size of $18 \times 21\ \mathrm{mm}^2$ and an active area of $3.4\ \mathrm{cm}^2$. The DBM is included in the central data taking since the beginning of 2015. First results are expected in the near future.

3. Rate studies

The PLT pilot run [17] provided the first experience with scCVD diamond-based pixel sensors in the LHC-environment. A FLUKA [20,21] simulation estimated the total integrated fluence experienced by the PLT sensors during the 2012 LHC run to be 5×10^{13} neutral hadrons/cm^2 and 5×10^{13} charged hadrons/cm^2 [22].

An unexpected pulse height dependence on incident particle flux was observed already in the beginning of the run, after the diamond sensors received a relatively low fluence of 1×10^{13} hadrons/cm^2. When the particle flux was increased from $\sim$400 Hz/cm^2 to $\sim$16 MHz/cm^2, the pulse height was observed to decrease for these scCVD sensors [17]. This behavior has prompted a study in several high rate beam tests and first results are published [23].

Several diamonds were prepared for this study. The scCVD and pCVD diamonds were irradiated to a fluence of $(5.0 \pm 0.5) \times 10^{13}$ neutrons/cm^2. These sensors were compared with a non-irradiated scCVD sample and one of the scCVD diamonds irradiated in the PLT pilot run. All samples had a thickness of $\sim$500 μm. Two different sensor configurations as described later were tested in a pion beam with a momentum of 250 MeV/c provided by the High Intensity Proton Accelerator [24, beam line piM1] at Paul Scherrer Institut (PSI). The pion flux could be varied between 1 kHz/cm^2 and 10 MHz/cm^2.

In these beam test campaigns pad and pixel detectors were tested. The diamond pad sensors had a single $3.5 \times 3.5\ \mathrm{mm}^2$ Cr/Au metalization on the front and backside plus an extra guard ring on one side. An ORTEC 142A preamplifier combined with an ORTEC 450 amplifier was used to amplify and shape the signals [25]. The waveforms were digitized with a DRS4 evaluation board [26] using a sampling rate of 700 MHz. The pixel detectors had a size of $4.5 \times 4.5\ \mathrm{mm}^2$ and were produced with an electrode size of $75 \times 125\ \mu\mathrm{m}^2$ and a pixel pitch of $100 \times 150\ \mu\mathrm{m}^2$. The sensor was bump bonded to the CMS pixel Read Out Chip ROC PSI46v2 [27] with an internal threshold of 3000–3500 e. In total $\sim$1000 pixels were connected to the ROC. The collected charge was integrated on an internal capacitance and digitized with an ADC. With the different setups the impact of the internal threshold and effects due to the different electric field configurations were studied. While pad detectors have a uniform electric field within the bulk material, the electric field of pixel detectors is focused around the pixelated electrodes.

A beam telescope based on CMS pixel ROC PSI46v2 with silicon sensors was used to test these detectors. The ROC provided a fast trigger signal [27] if a hit was registered. The coincidence of the triggers from the two outermost planes was used for data acquisition decision. When running in the pad configuration the telescope was used to provide a scalable trigger with one silicon plane in front and one silicon plane in the back of the Device Under Test DUT. In the pixel configuration a total of six planes was used. The two outer planes were silicon reference detectors providing the trigger signal. The four inner detectors were diamond detectors. All silicon and diamond detectors, but the detector under study, were used for tracking. Pictures of both configurations are shown in Fig. 2.

PAD detectors. The shaped pad detector pulses have a peaking time of approximately 200 ns and return to the baseline in 500 ns. The pulse height of these signals was extracted from the waveform of the DRS4 board by summing the digitized waveform for 75 ns around the peak position. Since the trigger timing within the waveform was constant within a run the peak position was assumed to be fixed within a run. For each sample the flux scan started at the lowest flux of $\sim$22 kHz/cm^2 going up in flux. The pedestal was either measured in a separate pedestal run,

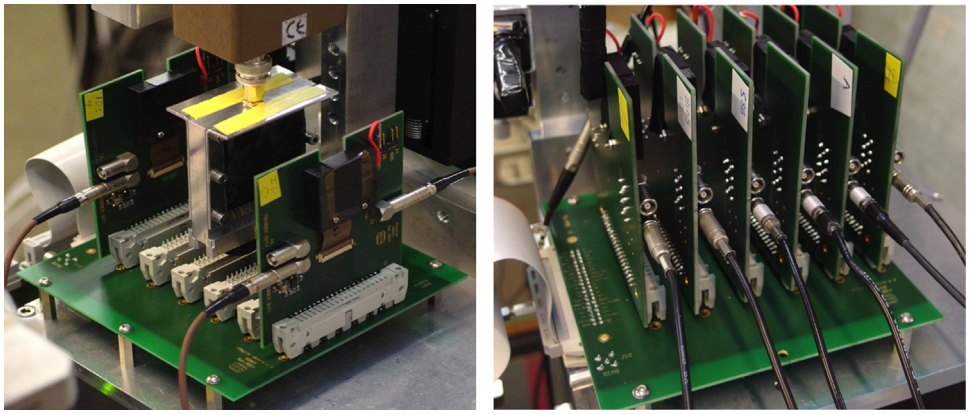

Fig. 2. The telescope for rate studies at PSI in the pad configuration (left) and in pixel configuration (right). In the pad configuration one can see the two silicon pixel planes for triggering and the pad detector in the middle. In the pixel configuration the pad detector is replaced by four pixel planes as DUT.

triggering on a fiducial region outside of the diamond or within the signal run by extending the trigger area beyond the active area of the diamond. To change the flux, the beam line was closed and only reopened after the collimator reached the new position. For each flux point the pulse height was extracted by subtracting the mean of the pedestal distribution from the raw signal integral.

Since the pulse heights of the various scCVD and pCVD diamond detectors differ from each other due to material properties and due to irradiation, the results are rescaled to simplify the comparison. For each diamond all pulse height distributions were rescaled with a diamond specific factor such that the mean of the pulse height distribution is equal to one for the lowest flux point. The statistical errors on the mean pulse height are below 1%. The systematic error on the mean calculation is estimated to be 3% by comparing different event selections and different runs of the same diamond.

The results of the measurement with pad detectors are shown in Fig. 3. It shows the change of the mean of the pulse height distribution as a function of the incident particle flux. The non-irradiated scCVD (top) and the neutron irradiated pCVD sample (bottom) do not show any pulse height dependence on flux while in the two irradiated scCVD samples a 10% drop is observed.

Pixel detectors. In the analysis of the pixel detectors a calibration method using internal calibration pulses [28] was used to convert the raw ADC values given by the pixel readout system to the collected charge measured in electrons. The two silicon planes and three diamond planes were used as a tracker to evaluate the fourth diamond detector. In the reference planes all adjacent pixel hits are merged to a cluster with a position calculated using charge weighting. The telescope was aligned using these clusters. Only if each of the reference planes had one and only one cluster, a straight line fit using these clusters was used to predict the hit position in the plane under test. Events with more than one pixel cluster in any plane were discarded from the analysis. All analyzed events had to fulfill requirements on the goodness of the track fit and the predicted hit position was required to be at least four pixels away from the edges of the plane under test.

For these events the pulse height of the event was defined as the sum of the charge of single pixel hits within a radius of four times the pixel pitch around the predicted intersection point (up to 9×9 pixels). This radius accounts for uncertainties on the predicted hit position due to multiple scattering and track resolution, as well as for charge sharing. The pulse heights for each plane under test were re-scaled with a diamond specific scale factor such that the mean of the pulse height distribution at the lowest flux was set to one. The systematic uncertainty on the average pulse height was estimated by a rate scan with a silicon

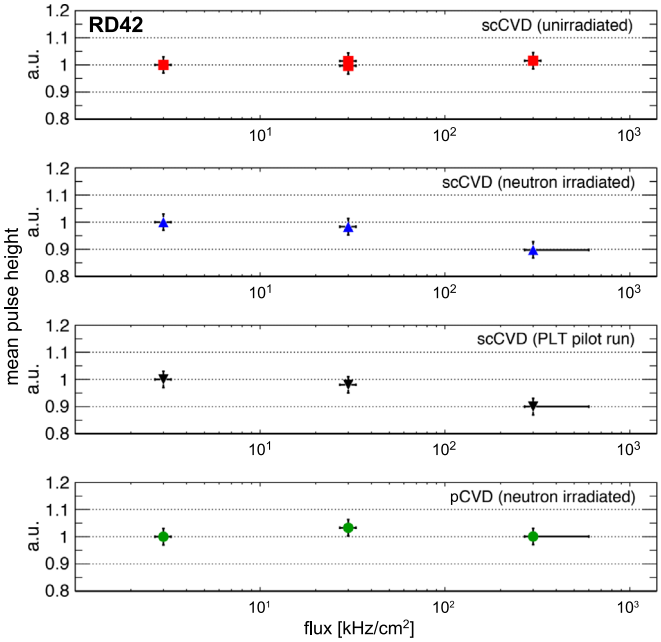

Fig. 3. The relative mean of the pulse height distributions for four different pad geometry diamonds versus the incident particle flux. The pulse heights of each diamond is scaled with constant factors such that the mean of the lowest flux is equal to one.

pixel detector as a plane under test. The differences in pulse height of this measurement resulted in an error of ~0.4%.

In Fig. 4 the pulse height for a scCVD diamond pixel sample used in the PLT pilot detector is shown. One can see that the mean pulse height decreases by 50% going from the lowest to the highest flux. This drop is consistent with the observation made during the PLT pilot run [17].

The average pulse height for a non-irradiated scCVD pixel diamond sensor as a function of incident particle flux is shown in Fig. 5. The data shows a small decrease of 5% between the lowest and highest flux. Meanwhile an increase of the mean cluster size with increasing flux was observed, as it is depicted in Fig. 6. This results in a reduction of charge per pixel and a lower average cluster charge due to the per-pixel threshold. The reason for the increasing cluster size is not yet understood and must be studied in more detail.

Summary and outlook. Non-irradiated scCVD diamonds do not show any significant flux dependence in the pixel and the pad geometries, while irradiated scCVD diamonds show a clear signal decrease with increasing flux in both geometries. Comparing these

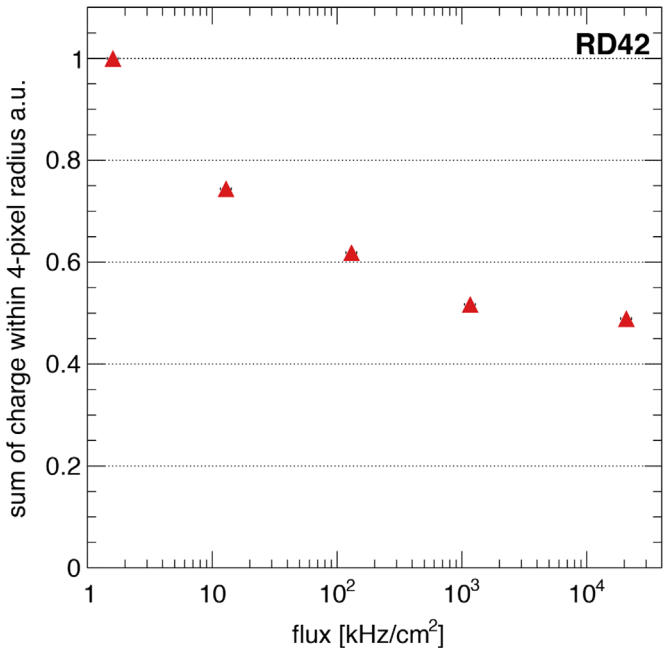

Fig. 4. The mean of the pulse height distribution versus the incident particle flux for a pixelated scCVD diamond irradiated in the PLT pilot run.

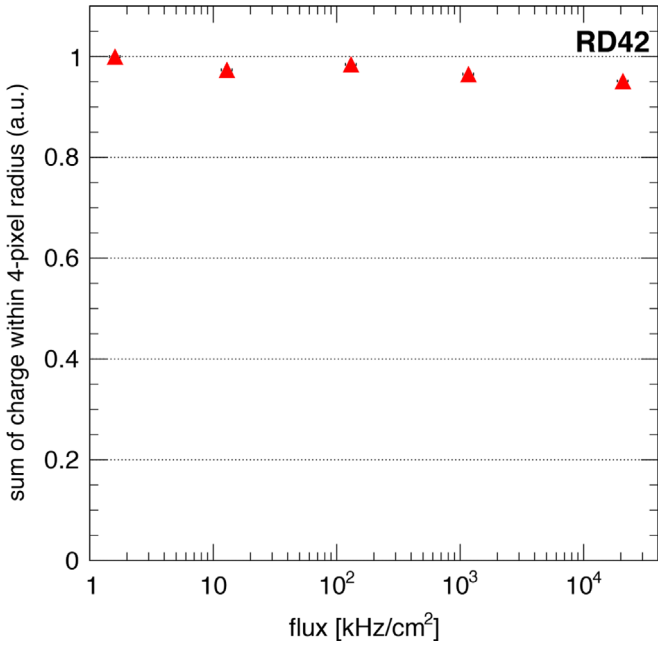

Fig. 5. The mean of the pulse height distribution versus the incident particle flux for a non-irradiated scCVD pixel detector.

decreases the observed effect is much more prominent in pixelated geometries compared to the pad geometries. This implies that the pixel readout threshold and the electrostatic field configuration are important factors when studying the flux dependencies with pixelated detectors. The results for pad detectors suggest that pCVD diamonds irradiated to 5×10^{13} neutrons/cm^2 have no dependence of the pulse height on particle flux.

The rate studies will continue with increased rates and higher irradiations expected at HL-LHC. In the first step measurements at rates up to 20 MHz/cm^2 are planed. This requires an update of the measurement setup. A new fast amplifier will improve the capability to measure pad detectors at these higher rates. The effect of

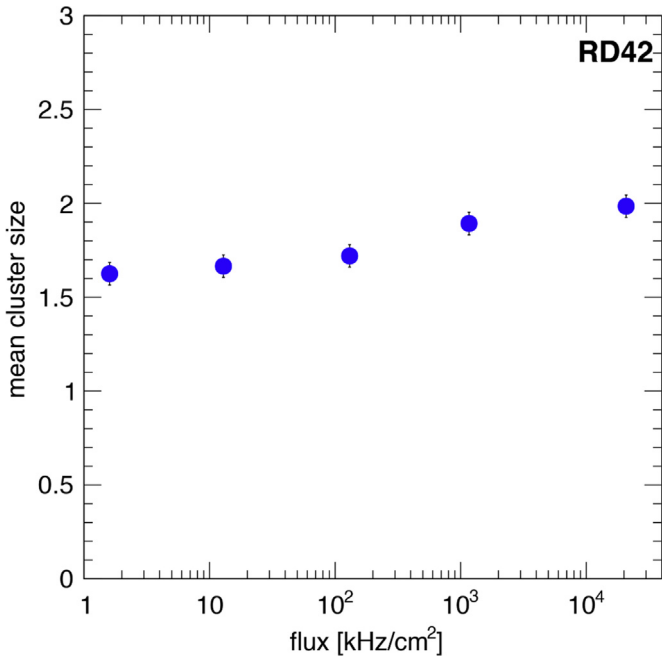

Fig. 6. The average cluster size versus incident particle flux for a non-irradiated scCVD diamond.

the internal threshold for the pixelated geometry can be reduced by employing the new CMS ROC PSI46digv2 [29].

4. 3D diamond detectors

In order to improve the charge yield for irradiated sensor materials, the concept of 3D sensors was proposed in [30], in which the drift path is reduced by placing the electrodes in the bulk material. Recently the production techniques and basic performance results for a prototype scCVD diamond sensor using a 3D read-out geometry were presented in [31]. These results are summarized below.

Fabrication. The sensor used was a 4.7×4.7 mm^2 scCVD diamond of 440 μm thickness [8]. In the initial qualification of the diamond as a pad detector using a ^{90}Sr source the sensor collected the full charge at a bias voltage of 450 V, and the full-charge collection was measured with this setup at 500 V to be 15770 ± 250 (stat) ± 350(calib+syst) e.

A femto-second laser with a wavelength of 800 nm [32] was used to create the 3D structure of electrodes by transforming the diamond lattice into a combination of diamond-like carbon, amorphous carbon and graphitic material [31]. This combination of materials is conductive and acts as electrodes. The diameter of the electrodes was estimated, in an inspection with a scanning electron microscope, to be about (6 ± 1) μm. In a resistance measurement of 52 electrodes a most probable resistance of 45 kΩ with a FWHM of 32 kΩ was extracted. This results in a resistivity of about (0.29 ± 0.10) Ωcm for a typical electrode.

In our 3D geometry cells were formed by four electrodes in the corners for biasing and one readout electrode in the middle. The cell size was 150×150 μm^2. The electrodes are referenced as bias columns for the ones in the corners of the cell and readout columns for the middle one, as illustrated in Fig. 7. There were three distinct areas on the diamond: one with the full 3D electrode geometry and metalization; one region, with identical metalization, but without the 3D electrodes (the so-called “3D phantom”); and a regular 2D strip-geometry with a pitch of 50 μm for performance comparison. Only the strip geometry uses a backplane metalization to apply the bias

voltage, while the 3D detector and the "3D phantom" were biased and read out from the same side. The layout of the mask can be seen in Fig. 7. For the readout a VA2 low-noise CMOS amplifier [33] with DC coupling was used. For the 3D detector and for the "3D phantom" all cells of one column were ganged together to one readout channel.

Beam test. The prototype detector was tested in a beam test at the H6 CERN-SPS beam line [34] with 120 GeV/c protons. Tracking was provided by a silicon tracking telescope [35] with two pairs of strip detectors in the front of the DUT and two pairs strip detectors downstream from the DUT. In each pair, one detector measures the horizontal coordinate (x), the other measured the vertical one (y).

After aligning the reference planes the final resolution of this tracking is 3–5 μm at the 3D detector surface. The readout was triggered by a coincidence of two Photomultiplier PMT reading out a single plastic scintillator.

The applied voltages for the measurements were 500 V for the 2D strip detector and 25 V for the 3D detector as well as the "3D phantom" detector. The leakage current of the strip detector was below 2 nA throughout the run, while the summed leakage current of the 3D detector and the "3D phantom" was below 1 nA.

Analysis. In the off-line analysis only events with one single track traversing the telescope were selected similar to the selection done for the rate-studies, corresponding to the final dataset of 250 000 events. The pedestal of each channel was calculated separately for each event using a sliding window algorithm. The raw signals were pedestal and common mode corrected. After these steps, the electronic noise was determined by the width of the pedestal distribution. It was measured to be 82 e for the planar strip detector, 92 e for the "3D phantom" and 95 e for the 3D detector. These relative sizes agree qualitatively with the expected order of the capacitance of the three geometries. In Fig. 8 the average of the measured charge within the full detector is plotted as a function of the predicted track position. The positions of the planar strip, the "3D phantom" and the 3D detector are marked on the two dimensional plane. One can see that a small part of the strip detector was not in the active trigger window of the scintillator and has no hits. Within the "3D phantom" an inhomogeneous charge collection can be observed. In the middle of the detector the pulse height is significantly lower than within the other two detectors. This is expected as the "3D phantom" acts like a pure surface device. In the regions close to the neighboring detectors charge is partially collected by the adjacent detectors, indicating that in these regions the electric field is distorted and therefore differs from the electric field of a pure surface device. In the 3D detector one can observe that some regions have a lower signal

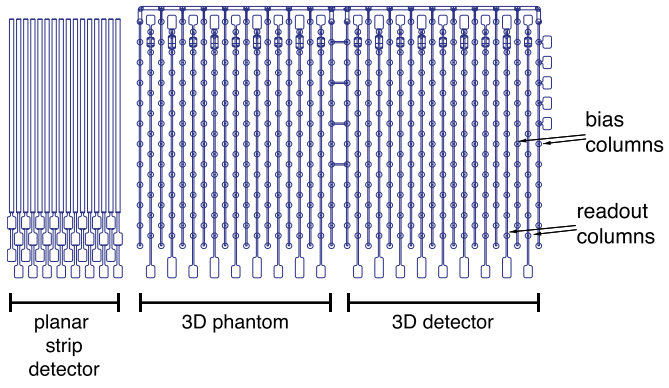

Fig. 7. The design of the metalization pattern with the three regions of planar strip detector, "3D phantom" and 3D detector as described in the text.

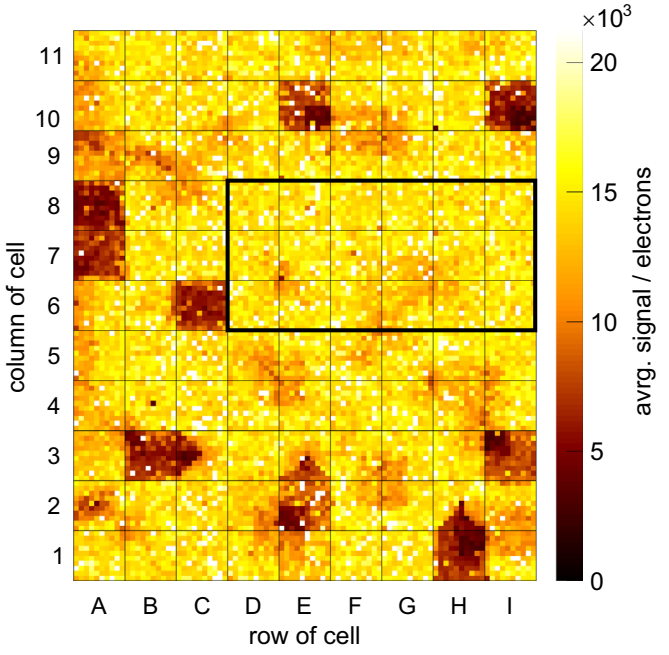

Fig. 9. The average cluster charge versus the predicted hit position for the 3D detector. The cell grid is overlaid to show the cell boundaries. A subset of adjacent cells with working readout columns is highlighted.

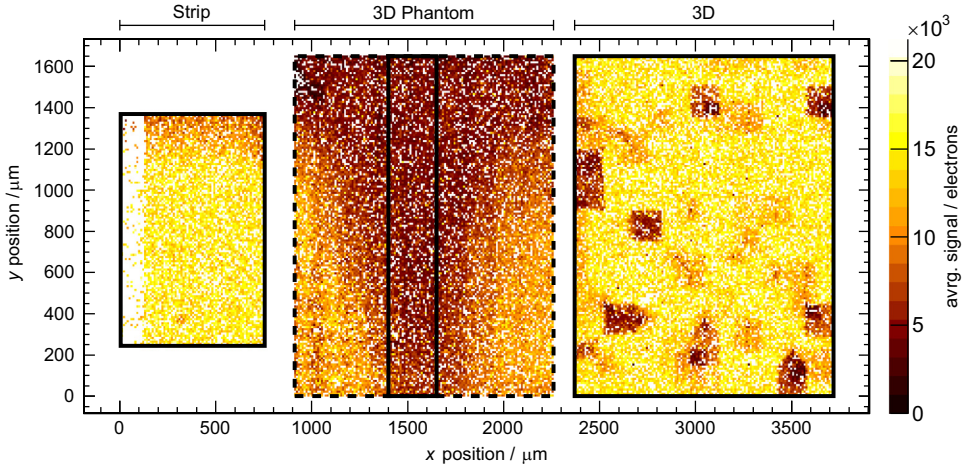

Fig. 8. Average charge within the prototype detector versus the predicted track position. In this plot charge is defined as the sum over all charges in the three detectors. The three detectors planar strip, "3D phantom" and 3D detector are marked.

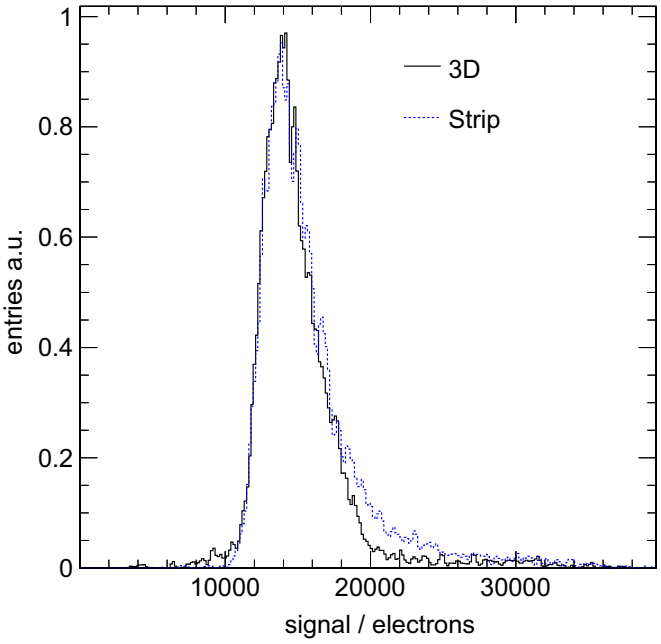

Fig. 10. Pulse height spectra of the planar strip and the 3D detector. For the 3D detector only events in the highlighted region of Fig. 9 were taken into account, events with a strong negative signal response were rejected.

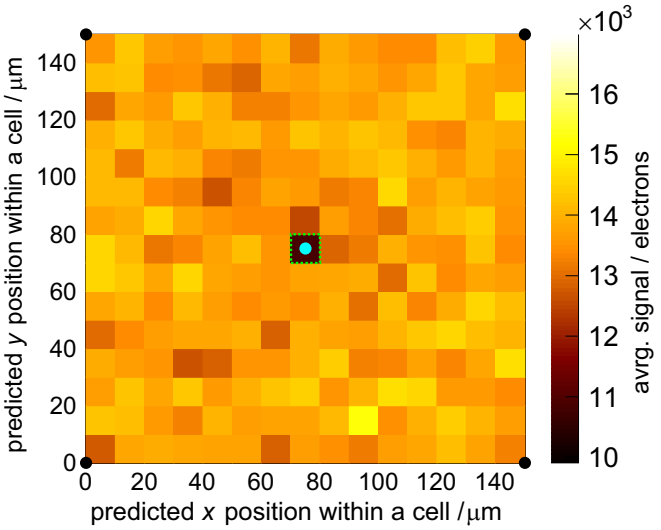

Fig. 11. Overlay of the signal collection within a cell versus the predicted hit position of the transversing particle. The position of the bias columns in the corner and the read out column in the middle is marked. The entry with readout is highlighted.

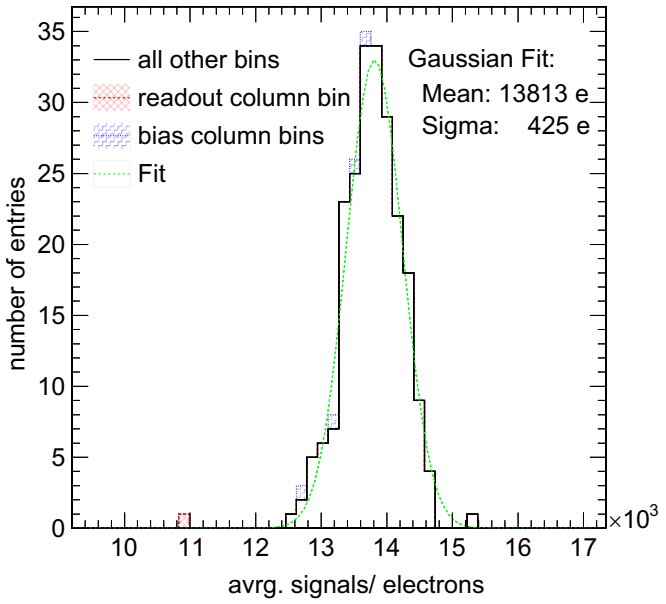

Fig. 12. The 1D distribution of the average cluster charge in the $10 \times 10\ \mu m^2$ bins within Fig. 11. The bins with readout and bias column are highlighted.

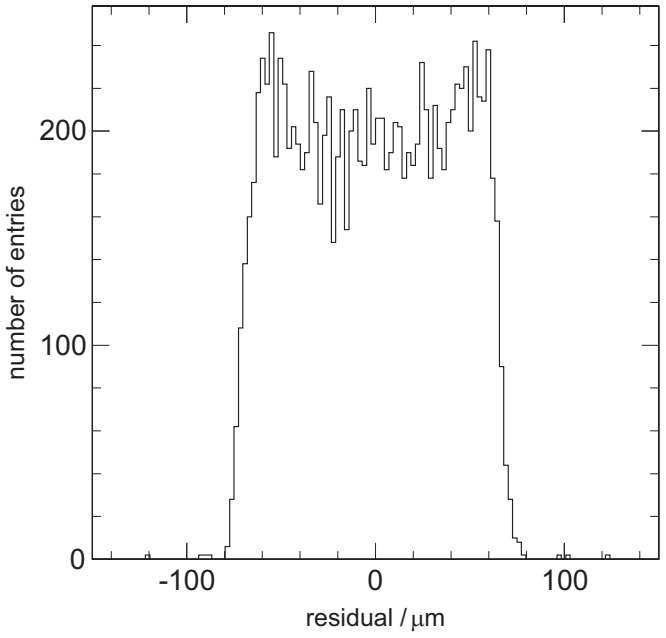

Fig. 13. Residual distribution of the reconstructed centroid position using the 3D detector. Events in the highlighted region of Fig. 9 are used. The width of the distribution is $\sigma(x) = (40.2 \pm 0.3)\ \mu m$.

response than the rest. The charge within these regions is similar to the charge collected in the "3D phantom". This can be explained by broken or disconnected readout columns.

Instead of considering the whole detector, a subset of 18 adjacent working cells was chosen. As seen in Fig. 9 in this subset all cells show an average signal response $> 10\,000$ e indicating that the readout columns were fully functional. Simulations with TCAD [36] show that broken bias columns can lead to a negative signal response in one of the adjacent cells. A selection criteria removing events with strong negative signal response was used to reduce the influence of those defective bias columns. Fig. 10 shows the response of the 3D detector and the planar strip detector when restricting events to the fiducial area defined above and applying the cut on negative signals. With the strip detector an average charge of 15 800 e and a most probable charge of 13 800 e is observed, while with the 3D detector the average charge observed is 15 000 e and the most probable charge observed is 13 900 e. The two spectra are consistent in their most probable value. Showing that the 3D detector reaches full charge collection at bias voltage of only 25 V. The distribution of the 3D detector does not exhibit the same long tail towards high values as the strip detector. This effect is not yet understood and will be studied in the future.

To study the signal response within the cell, each cell of the 3D detector was divided into bins of $10 \times 10\ \mu m^2$. The distributions of all cells with a working readout column were overlaid. Fig. 11 shows the average signal response as a function of the predicted hit position within the cell. In total 90 cells, which have a average

signal response above 10 000 e, are used for this measurement. The distribution of the average pulse height in the bins within the overlay is plotted in Fig. 12, the bins containing the readout and bias columns are highlighted. One can see a significant reduction in the average cluster charge for the bin containing the readout column. This can be explained by a lower signal response for particles transversing the electrode. By excluding bins containing either a readout or bias column, the distribution of the average collected charge across the cell can be fitted with a Gaussian. This fit has a mean of 13 820 e and standard deviation of 422 e, corresponding to a relative width of 3%, which indicates a uniform charge collection across the cell.

In Fig. 13 the residual distribution of the predicted hit position and the calculated position is shown. The position was calculated using the charge centroid of the three strips around the strip with the biggest pulse height in the detector. It exhibits a flat top distribution with a standard deviation of $\sigma(x) = (40.2 \pm 0.3)$ μm. Comparing this with the digital resolution of $\sigma_{dig} = 43.4$ μm for the 150 μm cell indicates no significant charge sharing between the 3D cells.

Outlook. New 3D detectors based on pCVD diamonds have been recently tested and the results are expected in the near future. The research on 3D detectors is continuing within the RD42 collaboration. The process of micromachining conductive electrodes in the diamond bulk will be optimized and an irradiation campaign for 3D diamond devices is planned.

5. Summary and outlook

The technology of diamond sensors is well established in the field of high energy particle physics. Several experiments are using diamond-based beam condition monitors. The first experiences in the use of diamond as pixelated tracking detectors has been accumulated within the CMS PLT pilot run. With the ATLAS DBM detector a new pixelated detector with the largest active area of diamond sensors was installed in LS 1 and is currently observing the first collisions in the LHC Run 2. It will be used to measure luminosity on a bunch-by-bunch basis.

With the new suppliers IIa Technology and II-VI Incorporated the situation on the market for detector grade CVD diamonds has improved. The quality, especially of finished pCVD diamond detectors, has improved strongly over the last years, the CCD of pCVD diamonds is reaching now 275–300μm.

The flux dependence of the pulse height observed in the pilot run of the PLT detector using pixelated scCVD sensors, triggered a major effort to understand the signal reduction. In several beam tests irradiated pad and pixel diamond sensors were studied to disentangle geometric effects. The flux dependence could be verified in a beam test with scCVD pixel sensors from the PLT pilot run. It was shown that the effect is smaller for scCVD pad sensors and cannot be observed for a neutron-irradiated pCVD pad sensor up to a particle flux of 300 kHz/cm^2. This study will be continued to validate this results to higher irradiation doses and higher fluxes, expected at the HL-LHC.

To enhance further the radiation hardness of diamond, 3D diamond sensors are being developed. The first 3D sensors using scCVD diamonds collects full charge at much lower bias voltage than the planar detector configuration on the same diamond, showing the potential as an interesting sensor technology. This effort is continued. New devices based pCVD diamonds were recently tested and studies of irradiated 3D detectors and tests with different bias voltages are planned.

Acknowledgments

The RD42 Collaboration would like to gratefully acknowledge the staff of the PRISM micro fabrication laboratory at Princeton University and in particular Bert Harrop for their excellent and dedicated efforts in the metalization and bump-bonding of diamond pixel detectors. We would also like to thank the beam line staff at the PSI High Intensity Proton Accelerator. We would like to especially thank Konrad Deiters, Manuel Schwarz and Davide Reggiani of PSI for their expert and invaluable assistance in carrying out the diamond detector tests. We would like to thank the test beam staff at CERN for allocating us the test beam time and for their help in setting up the excellent beam conditions. We would especially like to thank Henric Wilkins and Horst Breuker, the test beam coordinators, as well as Edda Gschwendtner, for their assistance in making our tests a success. The research leading to these results has received funding from the European Commission under the FP7 Research Infrastructures project AIDA, Grant agreement no. 262025 and under Horizon 2020 research and innovation program under Grant agreement no. 654168. This work was partially supported by the Swiss National Science Foundation Grant #20FL20_147466 and ETH-Grant 45 12-1. We would like to acknowledge support from the US Department of Energy through Grant DE-SC0010061.

Appendix A. RD42 author list

M. Artuso[22], F. Bachmair[26], L. B̈ani[26], M. Bartosik[3], J. Beacham[15], V. Bellini[2], V. Belyaev[14], B. Bentele[21], E. Berdermann[7], P. Bergonzo[13], A. Bes[30], J-M. Brom[9], M. Bruzzi[5], M. Cerv[3], C. Chau[18], G. Chiodini[29], D. Chren[20], V. Cindro[11], G. Claus[9], J. Collot[30], S. Costa[2], J. Cumalat[21], A. Dabrowski[3], R. DÁlessandro[5], W. de Boer[12], B. Dehning[3], D. Dobos[3], C. Dorfer[26], M. Dünser[3], V. Eremin[8], R. Eusebi[27], G. Forcolin[24], J. Forneris[17], H. Frais-Kölbl[4], K.K. Gan[15], M. Gastal[3], M. Goffe[9], J. Goldstein[19], A. Golubev[10], L. Gonella[1], A. Gorišek[11], L. Graber[25], E. Grigoriev[10], J. Grosse-Knetter[25], B. Gui[15], M. Guthoff[3], I. Haughton[24], D. Hidas[16], D. Hits[26], M. Hoeferkamp[23], T. Hofmann[3], J. Hosslet[9], J-Y. Hostachy[30], F. Hügging[1], H. Jansen[3], J. Janssen[1], H. Kagan[15], K. Kanxheri[31], G. Kasieczka[26], R. Kass[15], F. Kassel[12], M. Kis[7], G. Kramberger[11], S. Kuleshov[10], A. Lacoste[30], S. Lagomarsino[5], A. LoGiudice[17], C. Maazouzi[9], I. Mandic[11], C. Mathieu[9], N. McFadden[23], G. McGoldrick[18], M. Menichelli[31], M. Mikuž[11], A. Morozzi[31], J. Moss[15], R. Mountain[22], S. Murphy[24], A. Oh[24], P. Olivero[17], G. Parrini[5], D. Passeri[31], M. Pauluzzi[31], H. Pernegger[3], R. Perrino[29], F. Picollo[17], M. Pomorski[13], R. Potenza[2], A. Quadt[25], A. Re[17], G. Riley[28], S. Roe[3], M. Sapinski[3], M. Scaringella[5], S. Schnetzer[16], T. Schreiner[4], S. Sciortino[5], A. Scorzoni[31], S. Seidel[23], L. Servoli[31], A. Sfyrla[3], G. Shimchuk[10], D.S. Smith[15], B. Sopko[20], V. Sopko[20], S. Spagnolo[29], S. Spanier[28], K. Stenson[21], R. Stone[16], C. Sutera[2], A. Taylor[23], M. Traeger[7], D. Tromson[13], W. Trischuk[18], C. Tuve[2], L. Uplegger[6], J. Velthuis[19], N. Venturi[18], E. Vittone[17], S. Wagner[21], R. Wallny[26], J.C. Wang[22], P. Weilhammer[3], J. Weingarten[25], C. Weiss[3], T. Wengler[3], N. Wermes[1], M. Yamouni[30], M. Zavrtanik[11].

[1]Universität Bonn, Bonn, Germany, [2]INFN/University of Catania, Catania, Italy, [3]CERN, Geneva, Switzerland, [4]FWT, Wiener Neustadt, Austria, [5]INFN/University of Florence, Florence, Italy, [6]FNAL, Batavia, USA, [7]GSI, Darmstadt, Germany, [8]Ioffe Institute, St. Petersburg, Russia, [9]IPHC, Strasbourg, France, [10]ITEP, Moscow, Russia, [11]Jožef Stefan Institute, Ljubljana, Slovenia, [12]Universität Karlsruhe, Karlsruhe, Germany, [13]CEA-LIST Technologies Avancees, Saclay, France, [14]MEPHI Institute, Moscow, Russia, [15]The Ohio State University, Columbus, OH, USA, [16]Rutgers University, Piscat away, NJ, USA, [17]University of Torino, Torino, Italy, [18]University of

Toronto, Toronto, ON, Canada, [19]University of Bristol, Bristol, UK, [20]Czech Technical Univ., Prague, Czech Republic, [21]University of Colorado, Boulder, CO, USA, [22]Syracuse University, Syracuse, NY, USA, [23]University of New Mexico, Albuquerque, NM, USA, [24]University of Manchester, Manchester, UK, [25]Universität Göttingen, Göttingen, Germany, [26]ETH Zürich, Zürich, Switzerland, [27]Texas A & M, College Park Station, [28]University of Tennessee, Knoxville, TN, USA, [29]INFN-Lecce, Lecce, Italy, [30]LPSC-Grenoble, Grenoble, France, [31]INFN-Perugia, Perugia, Italy.

References

[1] CERN, HL-LHC: High luminosity large hadron collider ⟨http://hilumilhc.web.cern.ch/⟩, November 2015.
[2] B.R. Vormwald, CMS Tracker Upgrades: R & D Plans, Present Status and Perspectives, Technical Report CMS-CR-2015-240, CERN, Geneva, October 2015.
[3] D. Hits, A. Starodumov, The CMS Pixel Readout Chip for the Phase 1 Upgrade, Technical Report, CMS-CR-2014-450, CERN, Geneva, December 2014.
[4] W. de Boer, et al., Phys. Status Solidi (a) 204 (9) (2007) 3004.
[5] H. Pernegger, S. Roe, P. Weilhammer, V. Eremin, H. Frais-Kölbl, E. Griesmayer, H. Kagan, S. Schnetzer, R. Stone, W. Trischuk, D. Twitchen, A. Whitehead, Charge-carrier properties in synthetic single-crystal diamond measured with the transient-current technique, Journal of Applied Physics 97 (7) (2005), http://dx.doi.org/10.1063/1.1863417.
[6] S. Zhao, Characterization of the electrical properties of polycrystalline diamond films (Ph.D. thesis), Ohio State University, 1994.
[7] D. Asner, et al., Nucl. Instrum. Methods A 636 (2011) S125, http://dx.doi.org/10.1016/j.nima.2010.04.096.
[8] Element Six Ltd, Properties of electronic grade CVD diamonds, Kings Ride Park, Ascot, Berkshire, UK ⟨http://www.e6cvd.com/cvd/page.jsp?pageid=349#4⟩, November 2014.
[9] II-VI Incorporated, CVD Diamond Substrates, 375 Saxonburg Blvd., Saxonburg, PA 16056-9499, US ⟨http://www.iiviinfrared.com⟩, October 2015.
[10] IIa Technologies Pte Ltd, IIa Diamond Properties, 65 Chulia Street, #38-02/03 OCBC Centre, Singapore 049513 ⟨http://2atechnologies.com/⟩, November 2015.
[11] H. Kagan, W. Trischuk, Radiation Sensors for High Energy Physics Experiments, John Wiley & Sons, Hoboken, New Jersey, USA, 2009, 207–226, (Chapter 9).
[12] A. Gorisek, et al., Nucl. Instrum. Methods A 572 (2007) 67.
[13] V. Cindro, et al., J. Instrum. 3 (2008) P02004.
[14] A. Bell, et al., Beam and radiation monitoring for CMS, in: IEEE NSS 2008, 2008, pp. 2322–2325.
[15] E. Bartz, et al., Nucl. Instrum. Methods B (Proc. Suppl.) 197 (1) (2009) 171.
[16] M. Domke, et al., Commissioning of the beam conditions monitor of the LHCb experiment at CERN, in: IEEE Nuclear Science Symposium Conference Record, 2008, pp. 3306–3307.
[17] S. Schnetzer, et al., Diamond sensors for energy frontier experiments, In: PoS Vertex2013, vol. 029, 2013.
[18] A.L.S. Angelis, et al., CASTOR: Centauro and Strange Object Research in nucleus–nucleus collisions at LHC, Technical Report hep-ex/0209008, September 2002.
[19] C. ATLAS, ATLAS Insertable B-Layer Technical Design Report Addendum, Technical Report, CERN-LHCC-2012-009, CERN-LHCC-2012-013: ATLAS-TDR-19-ADD-1, CERN, Geneva, May 2012.
[20] G. Battistoni, et al., The FLUKA code: description and benchmarking, in: AIP Conference Proceedings, vol. 896, 2007, pp. 31–49.
[21] A. Ferrari, et al., FLUKA: a multi-particle transport code (program version 2005), CERN, Geneva, 2005.
[22] S. Müller, W. Boer, T. Müller, The beam condition monitor 2 and the radiation environment of the CMS detector at the LHC (Ph.D. thesis), Karlsruhe U., Karlsruhe, presented on 14 January 2011, 2011.
[23] R. Wallny, et al., J. Instrum. 10 (07) (2015) C07009.
[24] Paul Scherrer Insitut, High Intensity Proton Accelerator (HIPA) ⟨https://www.psi.ch/rf/hipa⟩, November 2015.
[25] ORTEC, Modular Electronic Instruments ⟨http://www.ortec-online.com/Solutions/modular-electronic-instruments.aspx⟩, November 2015.
[26] S. Ritt, DRS4 evaluation board ⟨https://www.psi.ch/drs/evaluation-board⟩, October 2015.
[27] K. Gabathuler, PSI46 Pixel Chip—External Specification, Technical Report, rev1, Paul Scherrer Institut, Villigen ⟨http://cmspixel.phys.ethz.ch/docs/psi46-readout-chip/psi46v2.pdf⟩, October 2015.
[28] C. Eggel, CMS pixel module qualification and search for $B_s^0 \to \mu^+\mu^-$ (Ph.D. thesis), ETH, Zurich, 2009.
[29] H.C. Kästli, Nucl. Instrum. Methods A 731 (2013) (2012) 88.
[30] S. Parker, C. Kenney, J. Segal, Nucl. Instrum. Methods A 395 (3) (1997) 328.
[31] F. Bachmair, et al., Nucl. Instrum. Methods A 786 (2015) 97.
[32] Coherent Inc., Libra series, data sheet ⟨http://www.coherent.com/downloads/LibraSeries_CoherentDataSheet_revC_May2013_4.pdf⟩, 2014 (accessed 22 December 2014).
[33] O. Toker, et al., Nucl. Instrum. Methods A 340 (1994) 572.
[34] CERN, Secondary beam areas of the PS, SPS machines, website: ⟨http://sba.web.cern.ch/sba/⟩, December 2014.
[35] C. Colledani, et al., Nucl. Instrum. Methods A 372 (1996) 379.
[36] Synopsis Inc, Sentaurus TCAD computational modeling, URL ⟨http://www.synopsys.com/home.aspx⟩, 2014.